Nuclear Inst. and Methods in Physics Research, A 1039 (2022) 167107

Contents lists available at ScienceDirect

Nuclear Inst. and Methods in Physics Research, A

journal homepage: www.elsevier.com/locate/nima

Thermal research of a single crystal tungsten target positron source for the STCF project in China

Ailin Zhang [a], Lechen Xu [a], Jiang Sun [b], Haiping Peng [a], Zijian Xiong [a], Yuxin Xiao [a], Qing Luo [a,*]

[a] State Key Laboratory of Particle Detection and Electronics, Department of Modern Physics, University of Science and Technology of China, Hefei 230026, China
[b] State Key Laboratory of Simulation and Effect for Intense Pulse Radiation, Northwest Institute of Nuclear Technology, Xi'an 710024, China

ARTICLE INFO

Keywords:
Accelerator sources and injectors
Positron sources
Thermal conductivity
Electron beam bombardment
Simulation

ABSTRACT

A new generation electron–positron collider, the Super Tau-Charm Facility (STCF), has been proposed in China. As a critical part of the STCF Linac, the positron source will use a 10 nC/50 Hz 1.5 GeV electron beam to bombard a single crystal tungsten target. To obtain a stable and reliable positron source with a long lifetime, this paper presents a molecular dynamics model to simulate the anisotropy of thermal conduction for single crystal tungsten. A series of electron beam bombardment experiments were performed, which confirmed that the anisotropy of thermal conductivity and the highest thermal conductivity for single-crystal tungsten is the close-packed crystallographic orientation of [111]. Scanning electron microscopy (SEM) and electron backscatter diffraction (EBSD) were used to study the recrystallization of the single crystal tungsten target. Finally, a new oscillation motional target system was designed for the STCF, and thermal simulation and moving speed optimization were performed.

1. Introduction

A new generation electron–positron collider, the Super Tau-Charm Facility (STCF), has been proposed in China [1–3] to study the asymmetry of matter–antimatter, the internal structure of hadrons, the nature of nonperturbative strong interactions, exotic particles and physics beyond the standard model. The STCF will have a luminosity greater than 0.5×10^{35} cm^{-2} s^{-1} and a center-of-mass energy region of 2–7 GeV (in the first phase). It is expected that its efficiency will be 50 times better than that of the currently operating BEPCII, which means that STCF faces a major challenge in constructing accelerators and detectors. The STCF will be very important scientifically and strategically not only for fundamental scientific research but also for the development of new technology and the cultivation of comprehensive expertise.

The general scheme of the accelerators is shown in Fig. 1. The injector system consists of an electron gun, a positron production system, electron and positron Linac sections, a damping ring and transfer lines connecting these systems to the main rings of the collider.

An efficient positron source is essential for the top-off operation and high luminosity of STCF. Tau-Charm physics requires that the energy of the STCF Linac must cover 1.0–3.5 GeV; thus, the electron beam energy that can always be obtained from Linac is only 1 GeV, which is too low for positron production. Considering the budget and space constraints, an extral-500 MeV Linac is designed for positrons. Therefore, the electron energy of the STCF for positron production is only 1.5 GeV, which is relatively low compared to that of FCC-ee [4], CEPC [5], and KEK [6], whose incident electron beam is more than 3 GeV.

The positron yield at the target exit was optimized by scanning the tungsten target thickness with Geant 4, which is shown in Fig. 2. The simulation results show that the best target thickness for 1.5 GeV electrons is 13 mm, and the positron yield is approximately 4, which is much lower than that of the 3 GeV and 4 GeV electron beams. Using the beam transmission simulation after passing through the preacceleration structure, the positron yield is only approximately 0.25 after damping is reduced to 0.15. To meet the first phase of STCF demand (1.5 nC for positron injection), at least a 10 nC/50 Hz electron beam is needed, which will be produced by a thermionic electron gun.

The positron yield and peak energy deposition density (PEDD) were simulated by Geant 4, as shown in Figs. 3 and 4. The main parameters of the positron source with amorphous tungsten target of STCF are summarized in Table 1.

To reserve upgrade space for the second stage of STCF, we need to obtain a higher yield under 1.5 GeV electron beam bombardment. Increasing the electron gun to more than 25 nC/50 Hz will produce an emittance growth problem; therefore, finding a way to increase the yield of positrons is a better option. It is necessary to optimize the capture and transmission efficiency of positrons and improve the positron yield from the target. Both KEK and CERN [7] have conducted a considerable amount of research on single crystal tungsten targets. The experimental results from KEK show that the positron

* Corresponding author.
E-mail address: luoqing@ustc.edu.cn (Q. Luo).

https://doi.org/10.1016/j.nima.2022.167107
Received 15 October 2021; Received in revised form 9 May 2022; Accepted 9 June 2022
Available online 2 July 2022

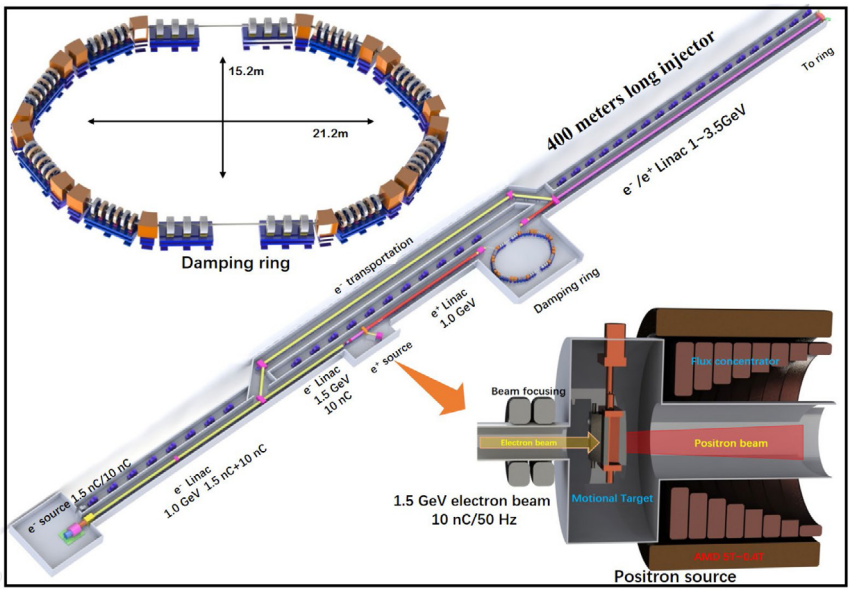

Fig. 1. The injector system of the STCF in China.

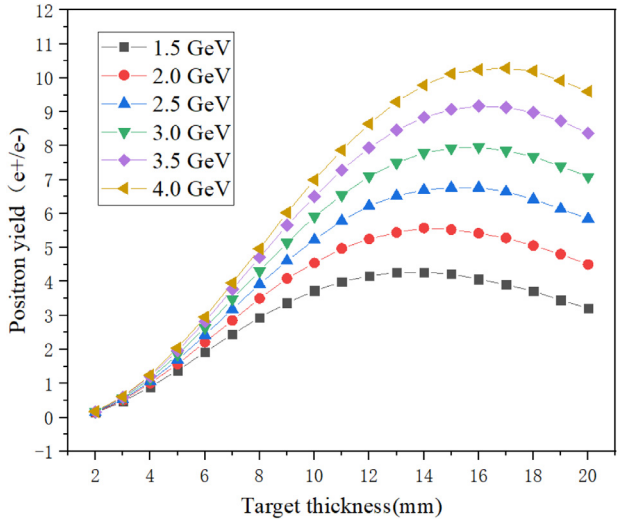

Fig. 2. Positron yield with different target thicknesses @ target exit with 1.5 GeV, 2.0 GeV, 2.5 GeV, 3.0 GeV, 3.5 Ge, 4.0 GeV electron beam, respectively.

Table 1
Main parameters of the STCF positron source.

Parameter	Phase 1	Phase 2
Electron bunch	10 nC	27 nC
Electron energy	1.5 GeV	1.5 GeV
Rep. rate	50 Hz	50 Hz
Deposited power	264 W	713 W
Magnetic field	5↘0.4 T	5↘0.4 T
Target thickness	13 mm	13 mm
Target material	Tungsten	Tungsten
e^+ yield @ after damping ring (e^+/e^-)	0.15	0.15
Peak Energy Deposition Density	10.5 J/g	28.4 J/g

yield increased by ~25% compared to a conventional tungsten plate with a thickness of 14 mm [8]. This improvement mainly comes from channeling radiation [9,10]. To obtain higher positron yields at 1.5 GeV electron beam hitting targets, single crystal targets can be tested.

Many target-based positron sources have been continuously used to provide a stable high-current electron beam for e^+e^- colliders such as BEPC II [11], International Linear Collider (ILC) [12], and SuperKEKB [13]. Tungsten has been considered the best candidate target material for positron transformation targets. However, melting and sputtering [14] often occur in tungsten under harsh work conditions. These damage phenomena are closely related to the thermal conduction of tungsten [15]. Transient heat loads caused by electron beam impact erode the target materials [16]. Therefore, it is important to research the thermal conduction of tungsten. The channeling radiation is very sensitive to the crystal structural change of the tungsten target; thus, the thermal effect of the single crystal under electron beam bombardment becomes very important. In this study, the irradiation damage caused by a pulsed electron beam will be systematically researched. Molecular dynamics simulations and experimental results were performed to study the thermal conductivity and recrystallization of a single-crystal tungsten target under pulsed electron beam bombardment, and a new motional-water-cooled target was designed to solve these problems.

2. Thermal conductivity of single crystal tungsten

Thermal conductivity is one of the three methods of heat transfer. It refers to the intrinsic ability of a material to transfer or conduct heat, which is mainly dependent on the contribution of electrons and phonons. According to the Wiedemann–Franz law [17], the contribution of electrons to the thermal conductivity of tungsten (172.7 W m^{-1} K^{-1} at 300 K) is estimated to be approximately eight times the contribution of phonons. However, irradiation damage to tungsten, such as the formation and growth of defects and atomic displacement, is directly related to lattice vibration. As a result, the contribution to thermal conductivity by phonons is more important to describe the damage mechanisms of positron target tungsten.

There are many experimental studies on the thermal conduction of tungsten materials [18]. However, many issues regarding heat conduction have not been resolved [19] such as the effect of lattice defects on the thermal conduction of metals. Molecular dynamics is a powerful method for studying microscopic thermal conduction processes by phonons [20–24]. The anisotropy of thermal conduction [25], size effect [26] and interface effect [27] on thermal conduction are the most important parts. The thermal conductivity by phonons can be calculated using either the equilibrium method [28] or nonequilibrium method [29] in molecular dynamics simulations. The Green–Kubo formula [30] can calculate the equilibrium time correlation function of

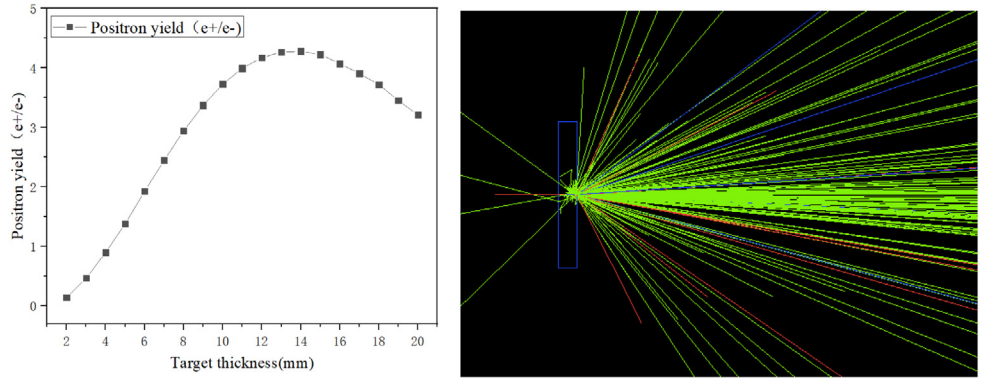

Fig. 3. Positron yield simulation by Geant 4. The positron yield simulation results with different target thicknesses @ target exit with 1.5 GeV electron beam (left), track simulation results with 1.5 GeV electron beam bombardment of a 13 mm tungsten target (right).

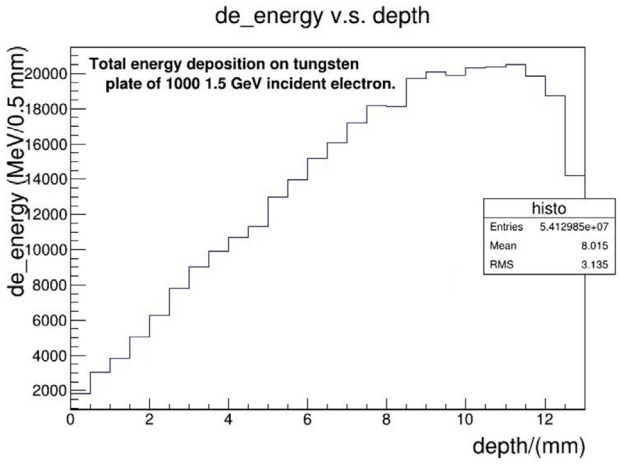

Fig. 4. Energy deposition density simulated by Geant 4.

the heat flux operator and thermal conductivity. The heat flux relies on imposing a temperature gradient across the simulation cell [31] or computing the temperature gradient by maintaining the heat flux across a particular crystal plane [32], which can be calculated by the nonequilibrium method.

In this study, the thermal conduction of tungsten will be calculated and analyzed by phonons with a nonequilibrium method, which is essential for research on the damage from electron beam. The simulation method, including the N-body potential function, calculation of thermal conduction and heat flux, and equilibrium cell parameters, will be described in this paper.

According to the classical Fourier heat transfer law, the thermal conduction can be presented as

$$k = \frac{J}{\partial T/\partial x} \tag{1}$$

where J is the heat flux along a special crystallographic orientation, and $\partial T/\partial x$ is the temperature gradient. Combined with the nonequilibrium method, the thermal conduction can be calculated.

The empirical N-body potential was used for tungsten by Finnis and Sinclair [33]. In the F–S potential, the total potential energy of the system is expressed as E=E

$$E = E_p + E_N \tag{2}$$

$+E$ where E_p is a conventional central pair-potential summation, and E_N is the N-body term [34].

Before the simulation, the equilibrium cell parameters should be calculated at different temperatures. The simulation cell consisted of $4 \times 4 \times 4$ unit cells, and the initial cell parameter of tungsten was 0.3165 nm. The third-order predictor–corrector algorithm was used to integrate the equations of motion with a time step of 10^{-15} s. The vacuum pressure was set to 10^{-5} Pa (experimental pressure).

The variation in the time-averaged volume and total energy of one atom with temperature is shown in Fig. 5. The thermal expansion coefficient at various temperatures was calculated with the volume–temperature curve under the first-order approximation [35].

The schematic representation of the three-dimensional periodic simulation cell is obtained from Ref. [36]. In this method, the heat flux is given by the expression:

$$J = \frac{\Delta\varepsilon}{2AMt} \tag{3}$$

where $\Delta\varepsilon$ is the kinetic energy difference between the atoms that exchanged every M steps (M is also called the heat exchange frequency), t is the molecular dynamics step, and A is the cross-sectional area. The physical meaning of the number 2 in this formula is that the heat flux can be conducted in both directions of y. The simulation of the heat flux is focused on the crystallographic orientation, and M is set to 10. The total simulation time is 100 ns (1×10^8 molecular dynamics steps). The frequency of phonon–phonon scattering events is far less than that in a fluid [37].

The temperature is calculated by the average kinetic energy of atoms for every mesh. The slab temperature is directly related to the kinetic energy (E_k) of the mesh.

$$E_k = \frac{1}{2}Nk_BT = \sum_i^N \frac{1}{2}m_i v_i^2 \tag{4}$$

where N is the atomic number, m_i is the mass of an atom, and k_B is the Boltzmann constant.

At the electron beam impact point, a very strong nonlinear temperature profile is observed, which is caused by strong scattering from the heat source or heat sink [38].

According to simulation studies, the heat flux has less influence on the thermal conductivity than the grain boundary. The close-packed [111] direction has the largest thermal conductivity in the crystallographic orientation. A sharp discontinuity in temperature appears when the grain boundary exists. The grain boundaries mainly come from the destruction of crystals resulting from electron beam impact, for which we will investigate the theoretical and experimental aspects.

The discontinuity of thermal conductivity for tungsten under electron beam bombardment is mainly caused by the destruction of the tungsten lattice, which takes two forms: displacement cascades of the tungsten lattice (transient energy deposition in general) and complete destruction and recrystallization of the tungsten lattice (very high transient energy deposition). Both of these effects exist in the future positron source for the STCF.

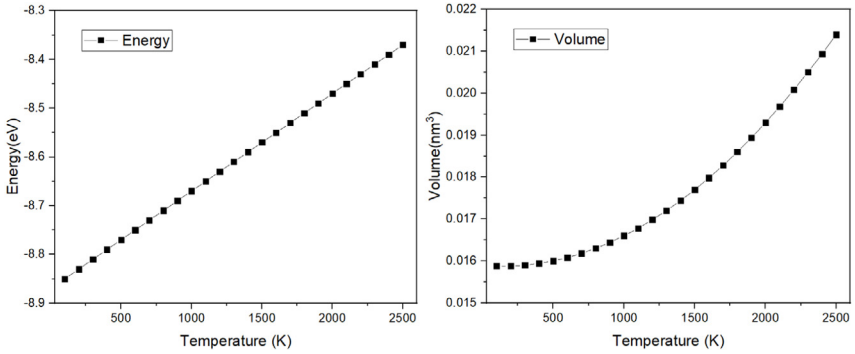

Fig. 5. Time-averaged total energy of one tungsten atom (left) and the time-averaged volume (right) as functions of temperature.

The Finnis–Sinclair [39–41] type potential was used in this model to simulate the interatomic potential for the electron beam radiation effect. The interaction potential between tungsten atoms and point defects is replaced by an interpolation function [42]. The effects of the primary knock-on energy and temperature on point defect production were calculated in this study.

The total potential energy of the Finnis–Sinclair model can be written as a sum of the central pair-potential and the N-body potential parts

$$E = \sum_{j>i} V\left(r_{ij}\right) - A\sum_{i}\sqrt{\sum_{j(\neq i)}\varphi\left(r_{ij}\right)} \tag{5}$$

where A is the potential parameter of the extended Finnis–Sinclair potential [43,44]. The charge density of atom i derived from the contribution of extranuclear electrons of atom j is expressed as $\varphi\left(r_{ij}\right)$. $V\left(r_{ij}\right)$ is the central pair-potential energy between atoms i and j, which can be expressed as

$$V(r) = \begin{cases} \frac{z_i z_j}{r}\sum_{k=1}^{4} b_k \exp\left[c_k r\left(Z_i^{0.23} + Z_j^{0.23}\right)\right] & r < r_{c1} \\ \exp\left(d_0 + d_1 r + d_2 r^2 + d_3 r^3\right) & r_{c1} \leqslant r < r_{c2} \\ (r-C)^2\left(C_0 + C_1 r + C_2 r^2 + C_3 r^3 + C_4 r^4\right) & r_{c2} \leqslant r < C \\ 0 & r \geqslant C \end{cases} \tag{6}$$

where b_k and c_k (k = 1, 2, 3 and 4) are the potential parameters of the ZBL universal potential [15], Z_i is the atomic number of atom i, and parameters C and C_i (i = 1, 2, 3 and 4) can be obtained from the extended Finnis–Sinclair potential [45]. The charge density function can be expressed as

$$\varphi\left(r_{ij}\right) = \begin{cases} B & r_{ij} \leqslant r_{c1} \\ B_0 + B_1 r_{ij} + B_2 r_{ij}^2 & r_{c1} < r_{ij} < r_{c2} \\ \left(r_{ij} - d\right)^2 & r_{c2} \leqslant r_{ij} < d \\ 0 & r_{ij} \geqslant d \end{cases} \tag{7}$$

where the parameters d, r_{c1}, r_{c2}, B and B_i (i = 0, 1 and 2) are fitted to the ZBL potential and the extended Finnis–Sinclair potential. These parameters can be found in Ref. [46].

Cascade simulations were performed with molecular dynamics techniques based on the Finnis–Sinclair potential. To integrate Newton's equations of motion for tungsten atoms, the predictor–corrector algorithm was used. The equilibrium cell parameters were calculated at the constant pressure and temperature ensemble at the target temperature before the cascade was initiated. Every equilibration time was 10 ps for each temperature step.

3. Simulation and experimental results of the thermal conductivity of single-crystal tungsten

A series of experiments were conducted to better understand the thermal conductivity, target damage, and lifetime of the electron beam-induced positron source. The experimental setup is shown in Fig. 6, including the electron beam, target, and water cooling. The electron energy used for the bombardment experiment was 200 MeV. The thickness of the tested tungsten target was 4 mm. Fig. 7 shows the simulation results of the energy deposition of a 200 MeV electron beam on the tungsten target and the experimental result of electron beam bombardment without water cooling (10 nC with 50 Hz). The damage to the tungsten target is severe after only 600 s of electron beam bombardment.

The experimental results show that the tungsten target will be destroyed in a very short time under the bombardment of a high-energy electron beam. The water flow in the experiment is estimated at 4 L/min; even with stronger water cooling, the tungsten target has no significant morphological damage, and the lattice structure can also be severely damaged. Many studies [47–49] have shown that pulsed beams, long time intervals, and sufficient water cooling will result in recrystallization of tungsten targets. The high energy deposited on tungsten in short periods of time will lead to remarkably high surface temperatures. When the temperature increased sufficiently, the tungsten easily underwent recrystallization and grain growth, resulting in significant property degradation and an increased ductile-to-brittle transition temperature [50]. Therefore, cracks are apt to form due to the high thermal stresses generated during transient events, which result in splitting, exfoliation and fatal destruction [51].

The first factor that affects recrystallization is the thermal conductivity. The thermal conductivity of single-crystal tungsten has strong anisotropy, which will be analyzed in this section. The thermal conductivities of various crystallographic orientations, [100], [110], [111], and [112], were calculated. The simulation cells include 25 000 × 5 × 4, 20 000 × 5 × 4, and 16 000 × 5× 4 constructed cells, and the total number of atoms is 5 × 10^7. The temperature of the whole system is set to 300 K by the initial thermalization, and the heat exchange frequency is M = 30. The results of thermal conductivity by phonons of various crystallographic orientations are shown in Fig. 8. The thermal conductivity of tungsten shows anisotropy to a certain extent. As the temperature increases, the difference in thermal conductivity of different crystal orientations becomes increasingly larger. Taking 2500 K as an example, the thermal conductivity of [111] is 9.14 W/m K, while that of [100] is only 3.56 W/m K.

The transient plane source (TPS) method can measure the in-plane thermal conductivity and through-plane thermal conductivity of anisotropic materials using a single test once the volumetric heat capacity is known [52,53]. The basic principle of the TPS method relies on a plane TPS probe that acts both as a temperature sensor and heat source. This probe consists of an electrically conducting pattern of thin nickel foil (10 μm) spiral-shaped embedded in an insulating layer usually made of Kapton (70 μm thick). The TPS element is located between the sample and a heat insulation, as shown in Fig. 9.

The TPS method offers some advantages compared to standard methods such as fast and easy experiments, a wide range of accessible thermal conductivities (from 0.02 to 400 W/m K), simple sample

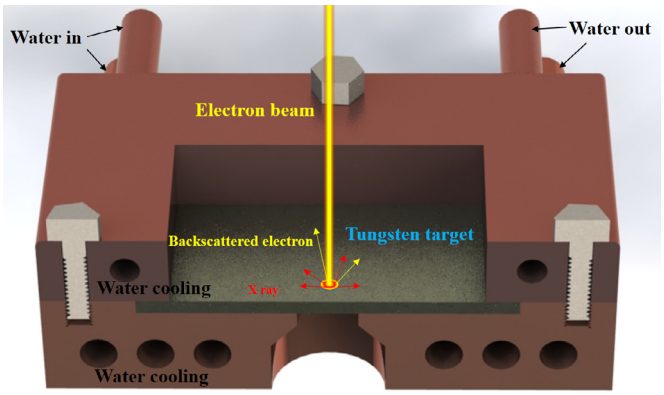

Fig. 6. Experimental setup of the electron beam target positron source.

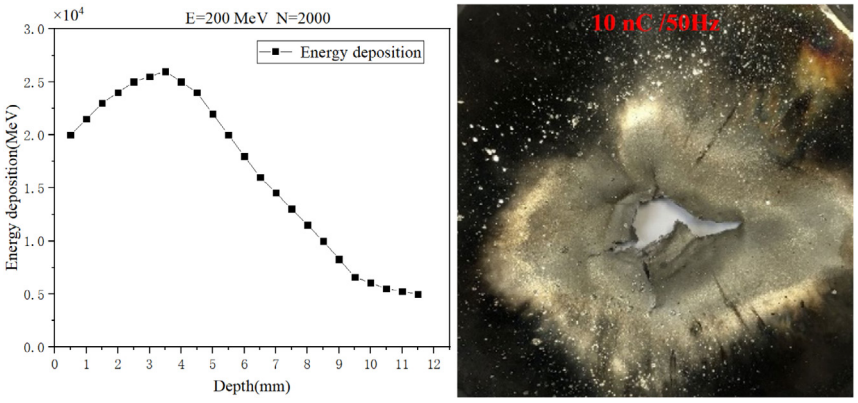

Fig. 7. Electron beam bombardment without water cooling [10 nC (50 Hz)]. (For 200 MeV electrons, the highest point of energy deposition is approximately 4 mm.)

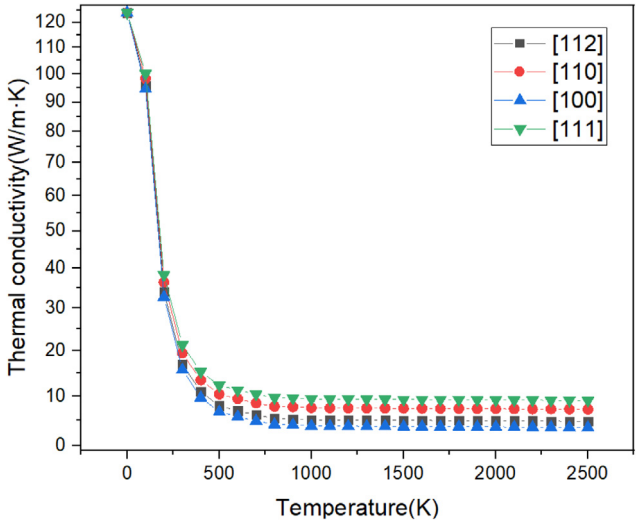

Fig. 8. Simulation results of the thermal conductivity for different crystallographic orientations at various temperatures.

preparation, flexibility in sample size and the possibility of performing local or bulk measurements by changing only the sensor diameter.

A constant electric power supplied to the sensor results in an increase in temperature $\Delta T(t)$, which is directly related to the variation in the sensor resistance $R(t)$ by the equation:

$$R(t) = R_0[1 + \alpha \Delta T(t)] \tag{8}$$

where R_0 is the nickel electrical resistance at the beginning of the recording (initial resistance), α is the temperature coefficient of resistance of the nickel foil, and $\Delta T(t)$ is the temperature increase of the sensor with time.

Assuming the conductive pattern of the tested single crystal tungsten plane is in the XY plane of a coordinate system, the temperature rise at point (XY) at time t is obtained by solving the equation for the thermal conductivity, which relates the change in temperature with time [54]. In the particular case of our sensor geometry, n concentric ring sources, the spatial average $\overline{\Delta T(\tau)}$ can be obtained through the equation [55,56]:

$$\overline{\Delta T(\tau)} = P_0 \left(\pi^{\frac{3}{2}} \cdot \lambda\right)^{-1} D(\tau) \tag{9}$$

where P_0 is the Bessel function, $D(\tau)$ is the geometric function characteristic of the number "n" of concentric rings, and $\overline{\Delta T(\tau)}$ is the temperature increase of the sensor expressed in terms of only one variable τ, defined as

$$\tau = \left(\frac{t}{\theta}\right)^{1/2}; \theta = a^2/\kappa \tag{10}$$

where t(s) is the measurement time from the start of the transient heating, θ is the characteristic time, which depends both on the parameters of the sensor and the sample, a (mm) is the sensor radius, and κ (mm^2/s) is the thermal diffusivity of the sample. The characteristic time needs to be in the range of 0.5–1.5 to guarantee that the theoretical assumptions are kept; thus, the heat flow is an ellipsoid of neither too high nor too low sphericity. Thermal conductivity can be obtained by fitting the experimental data to the straight line given by Eq. (9).

The TPS method was used to measure the thermal conductivity of a single-crystal tungsten target when single-electron pulses with different charges bombard the crystal tungsten targets of different crystallographic orientations. Because of the limitations of the experimental

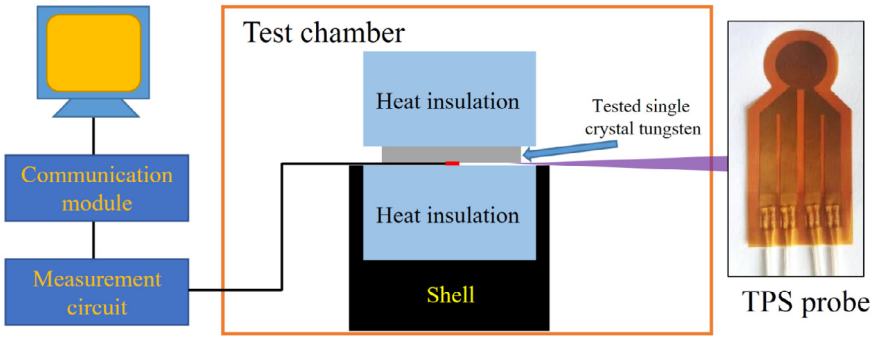

Fig. 9. Experimental diagram of the thermal conductivity measurement using the TPS method.

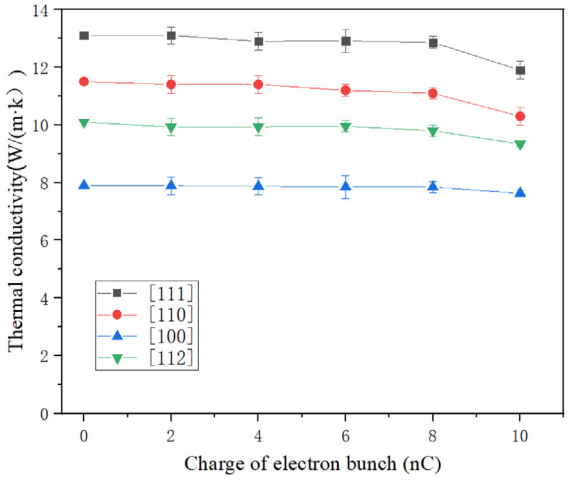

Fig. 10. Experimental measurement results of thermal conductivity for different crystallographic orientations.

conditions, the maximum charge of the electron bunch can only reach 10 nC, and the electron energy is only 200 MeV. The thickness of the single-crystal tungsten target is 100 mm × 100 mm × 4 mm. The diameter of the TPS probe is only 5 mm, which just covers the range of electron beam bombardment. Each sample was measured five times for thermal conductivity and then averaged. Fig. 10 clearly shows that the thermal conductivity in the [111] direction is much higher than that in the [100] direction.

Fig. 10 shows that thermal conductivity exhibits little change when the charge is below 8 nC and has a small drop at 10 nC. This result shows that the single-shot electron beam bombardment has a significant effect on the surface of the single-crystal tungsten target but has smaller effect on the internal structure of the single-crystal tungsten target. The possible reason for this result is that there is no energy accumulation by single-shot electron beam bombardment, and the internal heat dissipation efficiency will be higher than that of the surface.

4. Recrystallization of single crystal tungsten under a pulsed electron beam

Recrystallization has a strong randomness and will disrupt the original lattice structure, which is detrimental to the single crystal structure. For a long operation time under recrystallization conditions, the grains will also become increasingly larger, and the crystal orientation will become increasingly chaotic [57]. It is necessary to perform research on the recrystallization of single-crystal tungsten targets, which is a key factor to ensure the positron yield of single-crystal tungsten targets.

Based on ref [58], the recrystallization temperature of tungsten was in the range of 900–1400 °C. The temperature of the recrystallization of tungsten is different under different heating conditions [59]. Therefore, the results of conventional heat treatment could not precisely indicate the actual behavior of tungsten under high-energy beam loads. The grain size is an important parameter related to the mechanical properties of tungsten materials. The smaller is the grain size, the lower is the ductile–brittle transition temperature (DBTT) of tungsten, the stronger its ability to resist crack initiation and propagation [60], and the better its thermal shock resistance during service. Recrystallization is full of randomness, which is difficult to describe with mathematical preparation. Grain growth will result in sharp discontinuity in thermal conductivity, and this phenomenon has been observed in the heat flow across Si grain boundaries by Maiti [61]. A very strong nonlinear temperature profile is observed near the region of grain boundaries, which results from the strong scattering caused by grain boundaries. Experimental studies have shown that under the bombardment of pulse repetitive heat flow, when irregular recrystallization occurs, the heat resistance and lifetime of the tungsten target will be significantly reduced. [62,63]. Ref. [64] provides a good model for the recrystallization of metal, which is challenging to apply to high-energy electron bombardment on tungsten targets because this model was developed for low-energy bombardment. Therefore, in this study, scanning electron microscopy (SEM) was used to analyze the recrystallization phenomena of tungsten. The target is water-cooled during all electron bombardment experiments.

A single pulsed electron beam was used to bombard the crystal tungsten target in the [111] crystallographic orientation. The energy of each pulse ranged from 0 to 10 nC. The SEM results are shown in Fig. 11. With increasing pulse charge, the surface damage of the crystal tungsten target became increasingly severe. Next, a multipulse experiment was performed (see Fig. 12).

A pulsed electron beam with different pulse structures but the same power was used to bombard the crystal tungsten target to study at what conditions recrystallization occurred. Fig. 13 shows the results of 4 types of pulse structures. All structures had the same bombardment time of 5 s. Recrystallization is helpful for the reconstruction of the flatness of the surface. The SEM results show that there was clear recrystallization on the surface at the time structure of 10 nC/1 Hz, slight recrystallization at 5 nC/2 Hz, and no recrystallization at 2 nC/5 Hz and 1 nC/10 Hz. This series of experiments shows that the main factor of recrystallization is not the average power of the bombardment electron beam but the relatively strong instantaneous power.

To study the effect of the number of pulses on recrystallization, experiments with 10 nC/1 Hz pulsed electron beams with different pulses are shown in Fig. 13. As a result, as long as two electron beams bombard the same point in a short period of time, recrystallization occurs; however, to obtain stable recrystallization, a sufficient number of pulses is needed.

To study the time characteristics of recrystallization, the charge of the electron pulse was fixed at 10 nC, and the total number of

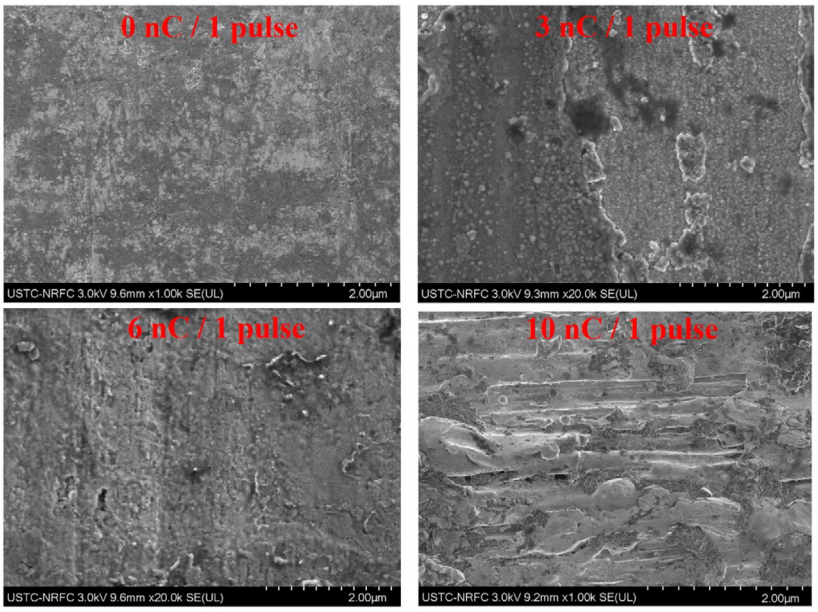

Fig. 11. Microscopic morphology of the crystal tungsten target bombarded by single pulsed electron beams with different charges.

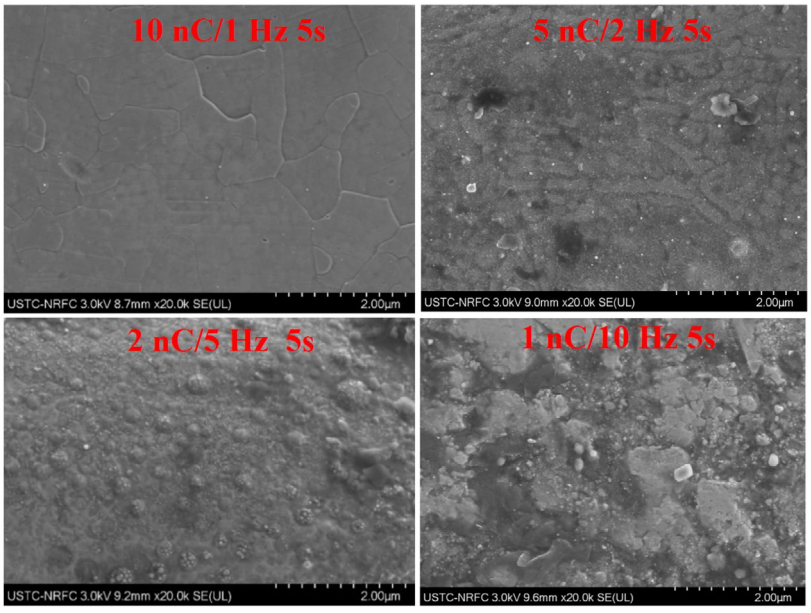

Fig. 12. Microscopic morphology of the crystal tungsten target bombarded by pulsed electron beams with different pulse structures but the same power.

pulses were fixed at five. Then, electron bombardment experiments were conducted at different time intervals. The SEM results are shown in Fig. 14. The recrystallization phenomenon at 10 nC/1 Hz is clear, and the surface after crystallization is also very smooth. There was also recrystallization at 10 nC/5 Hz, but obvious cracks appeared on the surface. The recrystallization at 10 nC/10 Hz is clear, but too many surface cracks start to overlap. The surface at 10 nC/20 Hz was completely damaged, and there was no recrystallization.

To better quantitatively analyze the recrystallization phenomenon, it is necessary to use electron backscatter diffraction (EBSD) [65]. The properties of recrystallized metals are dependent upon microstructural features such as grain size and crystallographic texture. The microstructures that evolve during recrystallization are a function of the deformed matrix, with nucleation and growth both being dependent upon local and neighboring lattice orientations and dislocation content. The deformed microstructure can be characterized by EBSD. HKL Nordlys with TESCAN MIRA 3LMH was used for electron backscatter diffraction in the paper, and the Oxford Instruments — HKL Channel 5 [66,67] was used to analyze data to obtain grain size and recrystallization ratio.

Fig. 15(a) shows the SEM results for 5 pulses of 10 nC/1 Hz electron beam bombardment in the [111] crystallographic orientations; (b) shows all grain results with EBSD, and (c) is the color bar for crystallographic orientation. Fig. 15 shows that under the bombardment of 5 pulses of 10 nC/1 Hz electron beam, although the surface is still smooth, the crystal orientation considerably changed, and only 31% of the grains in the [111] crystallographic orientations remained unchanged, which means that 69% of the [111] crystallographic orientations disappeared because of the crystallization effect.

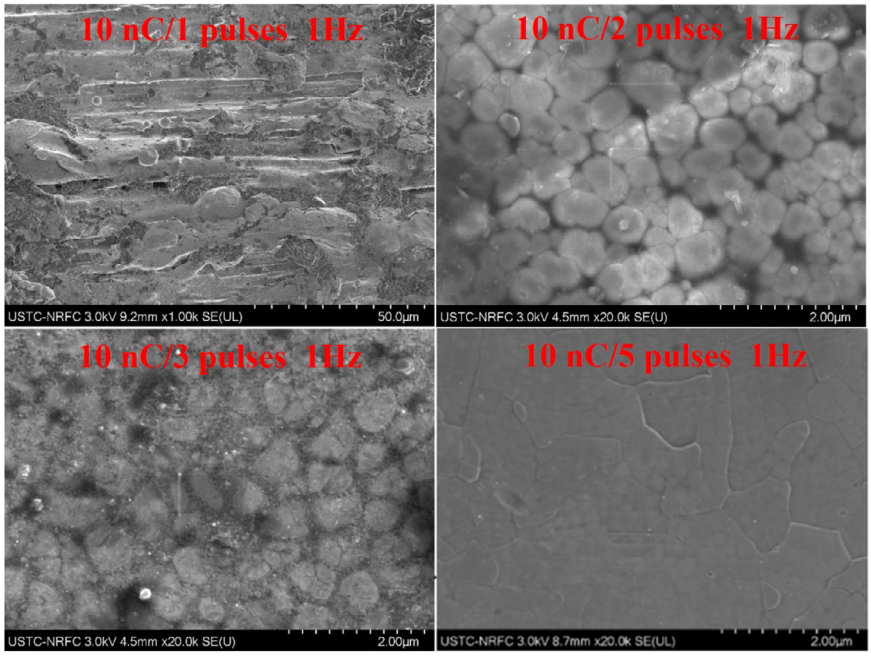

Fig. 13. Microscopic morphology of a single-crystal tungsten target bombarded by 10 nC/1 Hz pulsed electron beams with different pulses.

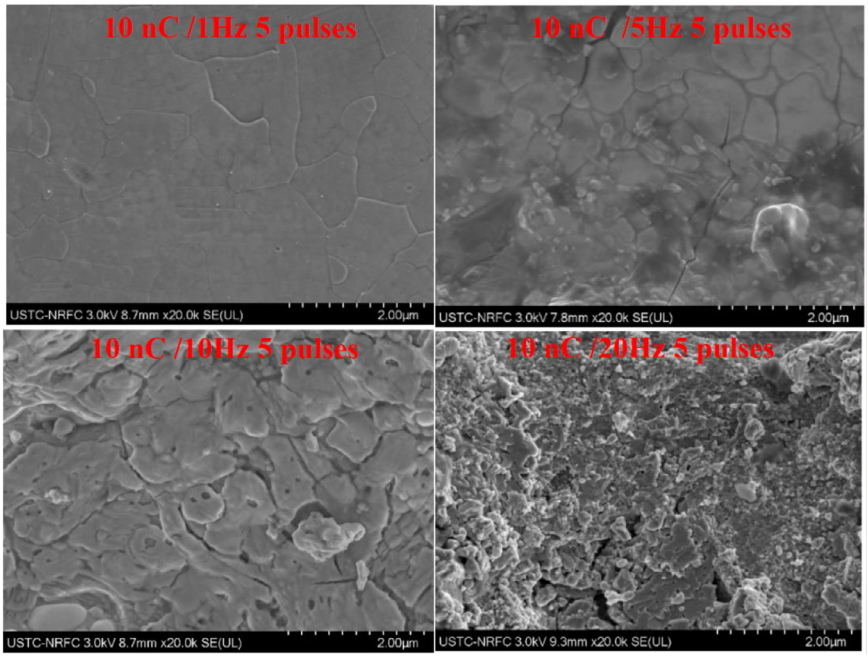

Fig. 14. Microscopic morphology of the crystal tungsten target bombarded by pulsed electron beams with different time intervals but the same charge.

Fig. 16 shows the thermal conductivity, grain size and degree of recrystallization results of single-crystal tungsten under the bombardment by different number of pulses at the same pulse frequency of 10 nC/1 Hz. It is observed that with the increase in the number of pulses, the thermal conductivity decreases, then increases, and stabilizes again because of recrystallization. The proportion of recrystallization increases, indicating that recrystallization is a cumulative phenomenon and slowly increases after reaching 74% (1%–26%). The recrystallized grain size also gradually increases and tends to increase steadily and slowly after reaching 13 μm. When the number of pulses exceeds 5, the thermal conductivity and grain size begin to stabilize. Of note, when there is bombardment by only a single pulse, recrystallization does not occur, the thermal conductivity changes, and the recrystallization rate (3%) is low, but the grain size still slightly increases.

Fig. 17 shows the experimental measurement results for the same pulse at different intervals. Fig. 14 shows that when the frequency exceeds 10 Hz, the surface of single-crystal tungsten will be seriously damaged, which is also shown in Fig. 17; that is, the crystal separation size of the single crystal significantly increases. However, under the bombardment of 1 Hz, 5 Hz, 10 Hz, 20 Hz, and 50 Hz electron beams, the thermal conductivity and the ratio of recrystallization change very little. When the frequency reaches 100 Hz, recrystallization will cause

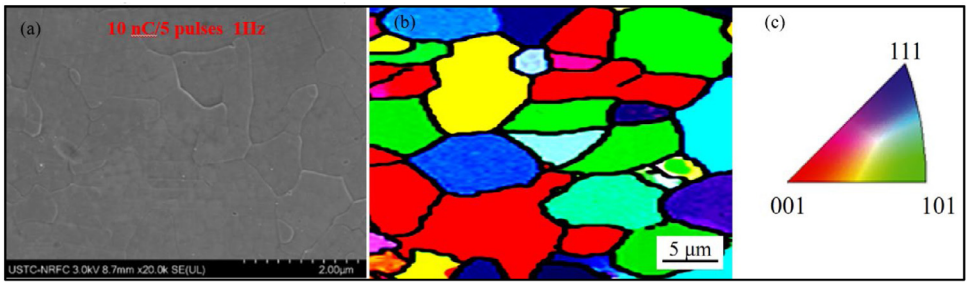

Fig. 15. SEM and EBSD results for 5 pulses of 10 nC/1 Hz electron beam bombardment in the [111] crystallographic orientation.

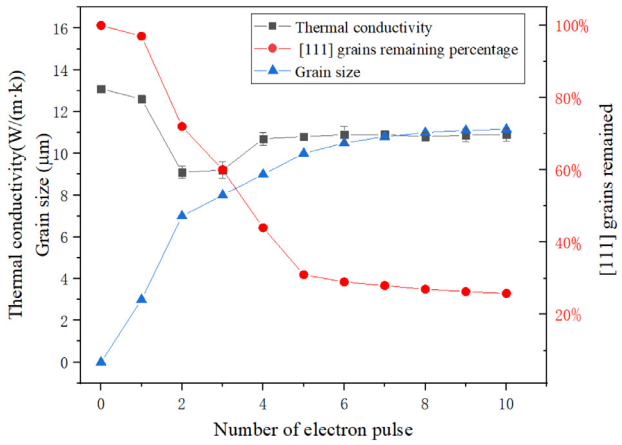

Fig. 16. Thermal conductivity, grain size and percentage of remaining [111] grains (degree of recrystallization) of the single-crystal tungsten target bombarded by 10 nC/1 Hz pulsed electron beams for different number of pulses.

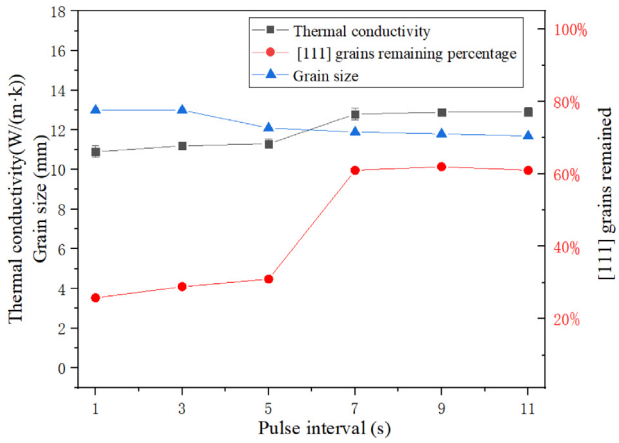

Fig. 18. Thermal conductivity and percentage of remaining [111] grains (degree of recrystallization) for a single-crystal tungsten target bombarded by 1000 electron pulses with different pulse intervals.

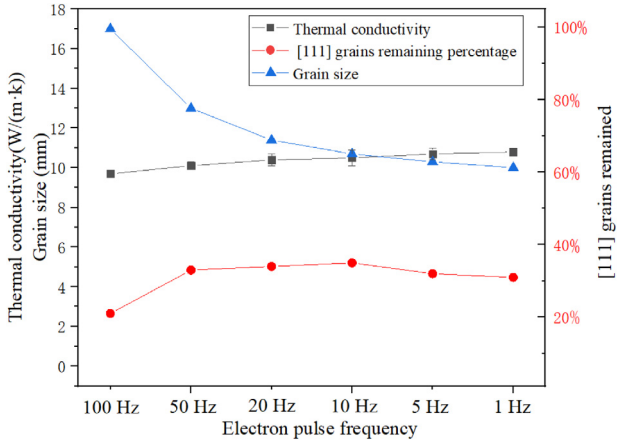

Fig. 17. Thermal conductivity, grain size and [111] grain remaining percentage (degree of recrystallization) results of a single-crystal tungsten target bombarded by 5 electron pulses with different pulse frequencies.

the thermal conductivity to considerably decrease. Of note, the SEM and EBSD measurements only focus on surface information, while thermal conductivity measurements include changes within the tungsten target. Damage on the surface does not necessarily represent a decrease in the thermal conductivity of the target. A more reliable approach is to estimate the change in the crystal structure of the entire tungsten target as a function of thermal conductivity. The thermal conductivity of amorphous tungsten measured by the TPS method is 9.32 W/(m k); as long as it is higher than this value, it means that there are still some [111] crystallographic orientations. This experiment suggests that the recrystallization phenomenon needs to be treated more carefully in the future when the STCF's 10 nC/100 Hz electron beam bombards single crystal tungsten targets.

Studies in Ref. [59] have also shown that the characteristic time of recrystallization for tungsten is also approximately 200 ms. Water cooling can reduce the average temperature well but does not prevent recrystallization because the water cooling point is far from the bombardment (approximately 25.7 mm in this case), and it is too far to prevent tungsten from transient high temperatures, leading to the appearance of the recrystallization temperature (900–1400 °C) between the pulse intervals.

Long-term bombardment experiments with longer pulse intervals were performed and are shown in Fig. 18. When the interval between pulses is more than 7 s, the accumulation of instantaneous heat becomes difficult, water cooling has enough time to remove the local instantaneous heat, the recrystallization temperature (900–1400 °C) may not last long enough, the recrystallization ratio will be greatly reduced, and the changes in thermal conductivity will decrease. The thermal conductivity of the [111] crystallographic orientation is much higher than that of other crystallographic orientations. Under the bombardment of electron beams at 7 s intervals, the thermal conductivity of the single-crystal tungsten target reaches 12.7 W/(m k), which is very close to 13.1 W/(m k) without bombardment, indicating that most of the single crystal in the [111] crystallographic orientation is maintained inside the target. The [111] crystallographic orientation of the single crystal is likely to be far greater than the percentage (63%) measured by EBSD from the surface. Overall, as long as the interval between pulses is sufficiently long, then it is as effective as a single electron pulse bombardment; even though the surface may have some damage, the internal structure is still intact.

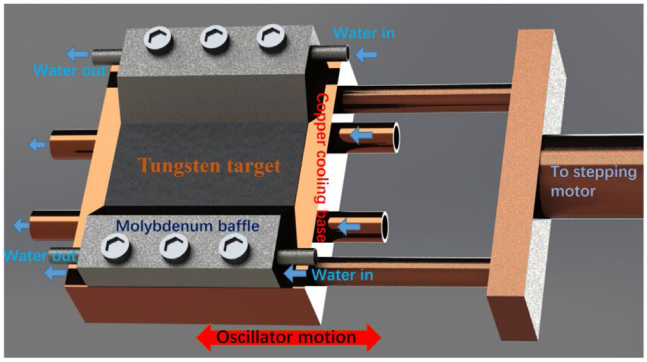

Fig. 19. A motional tungsten target with strong water cooling for the STCF positron system.

5. New target design and thermal optimization

In a single-crystal tungsten target positron source, the direction of the incident electron beam relative to the lattice structure is the key factor in the channeling radiation, which will require great stability on the single crystal structure under electron bombardment. Previous experiments have shown that when two electron beams repeatedly bombard a point in a short period of time of less than 7 s, recrystallization will strongly occur, and recrystallization can be significantly suppressed only when the electron beam interval exceeds 7 s, which is clearly insufficient for the e^+ e^- colliders' injector. To solve the pulse interval and instantaneous heat dissipation problem, moving the target and rotating the target can be a good option.

A rotating target was developed for an ILC positron source. This target is a novel idea and can solve the heat dissipation problem very well, but the cooling of the rotating target is a complicated issue. Whether water-cooled or air-cooled, the sealing of rotating mechanical structures is a complicated problem [68]. The Argonne National Laboratory proposed a new idea by sliding contact pads to cool ILC positron targets [69]. For sliding contact, the heat transfer efficiency cannot be guaranteed. A new repeated oscillation motional target with stronger water cooling (shown in Fig. 19) was designed at the University of Science and Technology of China (USTC). In the case of a moving target, water cooling is easier to add, and the size of the target is relatively small, which is 350 mm ×350 mm ×13 mm. The beam will not repeatedly bombard one place, which is equivalent to increasing the bombardment pulse interval and can even prevent disorderly recrystallization.

The coupled thermal–electrical finite element (FE) model was defined in the ANSYS environment to virtually design and optimize the cooling and motion systems. Thermal radiation was handled according to the ANSYS Radiosity Solver method. The thermal radiation was calculated as a heat flow rate vector and added to the surface of the materials. The entire target was subjected to a convection load representing the vacuum (1×10^{-5} Pa) case. The charge of each bunch is 10 nC, taking into account the needs of the first stage of STCF; the frequency is set at 50 Hz, and the energy is set at 1.5 GeV. The bombardment point is set at 4 mm. The molybdenum baffle and the copper base connection were subjected to a convection load representing water cooling, which is assumed to be 500 W/m^3°C. The motional target moves at a speed of 15 mm/s. The simulation results of the static target compared with the motional target (right) are shown in Fig. 20. The static target has a temperature greater than 930 °C, while the temperature on the motional target is less than 360 °C. For the moving target, the instantaneous temperature of the surface is greatly reduced, which also prevents the electron beam from repeatedly bombarding a point in a short period of time so that the recrystallization phenomenon can be effectively controlled. The positron yield growth from channeling radiation will have a longer lifetime. The new target design has tungsten clamped to the copper heat sink, and perfect results have been obtained by thermal stress simulation analysis; however, in reality, the obtained results may be somewhat different because thermal gradients may cause tungsten to deform and lose contact with copper, which will be verified in future experiments.

The results in Fig. 20 are simulated by ANSYS without considering the considerable changes in thermal conductivity at different crystallographic orientations and different temperatures. Therefore, we manually added the thermal conductivity results obtained in Fig. 8 to the engineering data in ANSYS and set up two new materials. A series of simulations were performed to study the effect of crystallographic orientation on temperature after different electron bombardments. The target is moved at a speed of 15 mm/s. The difference between the thermal simulation results considering and not considering the influence of the crystallographic orientation on the thermal properties is shown in Fig. 21. After considering the crystallographic orientation, the obtained temperature is higher than when it is not considered in the high-temperature section. In the low-temperature section (less than 1600 °C), the thermal conductivity of the [111] crystallographic orientation is lower than when the crystallographic orientation is not considered, and the [100] direction is always the highest.

The moving path of the target is 200 mm. When the target moves to both ends, it needs to be turned back, which will cause the position at the edge of the target's moving path to be irradiated twice in a shorter time than the middle position. The moving speed of the target should be faster at both ends of the moving path to obtain a more uniform temperature distribution. To reduce the influence of the foldback movement at both ends of the target movement area, a movement scheme was designed, as shown in Fig. 22. The speed range of the target is 15~25 mm/s. Such speed distribution will finally be realized by stepper motor programming. The movement at both ends is accelerated, and the maximum temperature of the bombardment point in this movement mode was simulated.

The abovementioned discussion is based on the ideal thermodynamic model. In reality, a high instantaneous temperature will always cause damage to the surface of the tungsten target in a small area; for example, during the SEM analysis, the surface considerably changes under single electron beam bombardment; however, as long as there is no repeated bombardment, there will be no recrystallization, the structure of the lattice will be maintained, and its thermal conductivity changes very little. However, as long as more than 2 electron pulses are bombarded at the same point, recrystallization will occur, the unidirectional lattice structure will be destroyed, the channeling radiation efficiency will be reduced, and the yield of positrons will likely decline. Clearly, the moving or rotating target can prevent the electron pulses from repeatedly bombarding the same spot in a short period of time, which can effectively reduce the recrystallization phenomenon and has a good effect on maintaining the channeling radiation. The oscillating motional target compared with the rotating target has great advantages in sealing problems, which have a stronger application prospect in long-term stable operation.

Table 2 Main parameters of the positron source of the STCF positron source with motional single-crystal tungsten target

We carried out the thermal deposition simulation calculation of single crystal, and obtained the main parameters of STCF positron in Table 2. For the second stage of the future STCF, a positron beam of 4 nC is expected. Based on the abovementioned moving target speed, a 1.5 GeV 23 nC/50 Hz electron beam is recommended so that the maximum temperature on the moving target is only 860 °C, which is lower than the recrystallization temperature of tungsten. If the single crystal tungsten target can increase the positron yield by 20%, then 23 nC can obtain positrons of 4.1 nC at a positron yield of 0.18 after damping ring, and the main parameters of the second stage of the STCF positron source are recommended, as shown in Table 2.

The work on motional targets has just begun, and there are many shortcomings. In the next step, we will complete the development of the

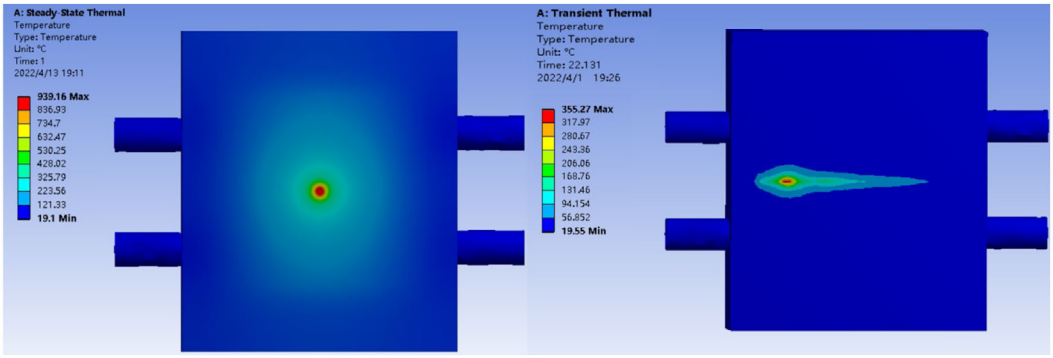

Fig. 20. Simulation results of the static target (left) with strong water cooling and the motional target (right) with the same water cooling.

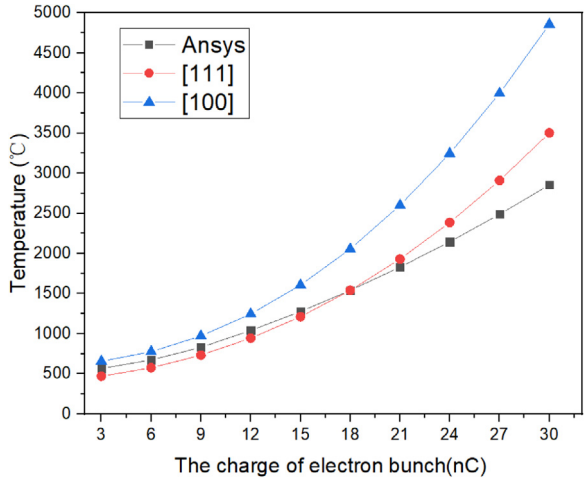

Fig. 21. Difference between thermal simulation results considering and not considering the influence of the crystallographic orientation on the thermal conductivity of various electron bunch charges. The repetition frequency is fixed at 100 Hz, and electron energy is fixed at 1.5 GeV. Triangle — the thermal conductivity comes from the molecular dynamics simulation of the [100] crystallographic orientation. Circle — the thermal conductivity comes from the molecular dynamics simulation of the [111] crystallographic orientation. Square — the thermal conductivity comes from the Ansys database for tungsten.

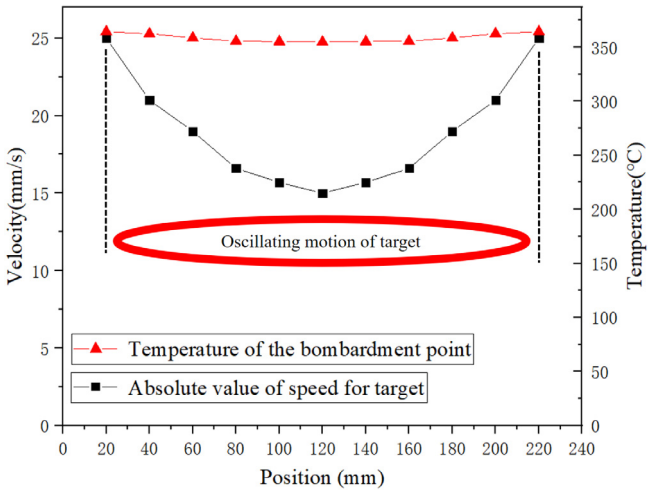

Fig. 22. Target moving speed optimization for recrystallization.

Table 2
Main parameters of the positron source of the STCF positron source with motional single-crystal tungsten target.

Parameter	Phase 1	Phase 2
Electron bunch	10 nC	23 nC
Electron energy	1.5 GeV	1.5 GeV
Rep. rate	50 Hz	50 Hz
Deposited power	291 W	670 W
Magnetic field	5↘0.4 T	5↘0.4 T
Target thickness	13 mm	13 mm
Target material	Tungsten	Tungsten
e^+yield @ after damping ring (e^+/e^-)	0.18	0.18
Peak energy deposition density	11.6 J/g	27.3 J/g

motional target and conduct the yield experiment with a higher energy electron beam. A positron spectrometer is under design, which will be used to analyze the yield and energy spectrum of the positron.

6. Conclusion

Tau-Charm physics requires that the energy of the STCF Linac must cover 1.0–3.5 GeV; thus, the electron beam energy that can always be obtained from Linac is only 1 GeV, coupled with space and financial constraints, the electron beam energy used for positrons can only reach 1.5 GeV, which is relatively low for the generation of positrons. To obtain a higher positron yield, the single crystal tungsten target would be a good choice. The single crystal target has great advantages in positron yield, but its lifetime and stability need to be studied carefully.

Recrystallization is a very common phenomenon in metals; it occurs at a relatively low temperature (only 900 °C for tungsten) and has a great destructive effect on the maintenance of single crystals. Therefore, it is necessary to study the thermal effect under pulsed electron beam bombardment. A molecular dynamics technique based on the Finnis–Sinclair potential model was proposed to calculate the anisotropy of thermal conductivity. The TPS method was used to measure the thermal conductivity of a single-crystal tungsten target. Both simulation and experimental results show that the thermal conductivity in the close-packed crystallographic orientation [111] is higher than that in other orientations, which is important for both target design and thermal effect analysis.

A series of electron bombardment experiments were launched to analyze the recrystallization phenomenon of single-crystal tungsten. These results show that with a 10 nC electron beam more than 5 pulses, the recrystallization effect occurs and severely damages its single crystal structure, only when the pulse interval exceeded 7 s, the recrystallization can be significantly suppressed. Such interval can only be achieved by moving or rotating the target. Therefore, an oscillation motional target is designed in USTC. The calculated results of the anisotropic thermal conductivity of the single-crystal tungsten were applied to the thermal simulation of the positron target, and the

speed of the target was also optimized to make the temperature of the bombardment point change uniformly with time, the instantaneous maximum temperature on the target is reduced from 940 °C to 355 °C, which is far lower than the recrystallization temperature of tungsten, thus greatly improving the lifetime of the positron source. In the next step, we will perform the experiments with a 1.5 GeV electron beam and a 13 mm single crystal tungsten with a motional target.

CRediT authorship contribution statement

Ailin Zhang: Conceptualization, Methodology, Software, Experiment, Writing – original draft. **Lechen Xu:** Data curation, Simulation, Experiment. **Jiang Sun:** Visualization, Investigation, Experiment. **Haiping Peng:** Supervision. **Zijian Xiong:** Software, Data curation, Simulation, Experiment. **Yuxin Xiao:** Software, Validation, Experiment. **Qing Luo:** Writing – review & editing.

Declaration of competing interest

The authors declare that they have no known competing financial interests or personal relationships that could have appeared to influence the work reported in this paper.

Acknowledgments

This work is supported by the National Natural Science Foundation of China (Grant Nos. 12105278 and No. U1832169), the Double First-Class University Project Foundation of USTC, China, and the Fundamental Research Funds for the Central Universities, China. We appreciate the help from the State Key Laboratory of Particle Detection and Electronics of USTC, China; and the supports from Collaborative Innovation Program of Hefei Science Center, CAS, China. The authors would like to thank Hefei Comprehensive National Science Center for their strong support. We expect the STCF to be an important part of the science center.

References

[1] D.R. Xu, W. Li, Q. Luo, W. Gao, J.Q. Lan, Proceedings of 10th International Particle Accelerator Conference, IPAC2019, Melbourne, Australia, 2019, pp. 643–645.
[2] Q. Luo, A.L. Zhang*, H.P. Peng, DA global model, IEEE Trans. Plasma Sci. 49 (6) (2021) 1848–1853.
[3] J.Q. Lan, Q. Luo, C. Zhang, W.W. Gao, Y. Xu, Y. Bai, Design of beam optics for a super tau-charm factory, J. Instrum. 16 (2021) T07001.
[4] Nucl. Instrum. Methods Phys. Res. B 240 (2005) 762–776.
[5] Radiat. Detect. Technol. Methods 3 (2019) 32.
[6] Proceedings of PAC07, THPMN030, Albuquerque, New Mexico, USA.
[7] X. Artru, V. Baier, K. Beloborodov, et al., Summary of experimental studies at CERN on a positron source using crystal effects, Nuclear Instrum. Methods Phys. Res. 240 (3) (2005) 762–776.
[8] New positron source with tungsten single-crystal at the KEKB injector linac, in: VII International Symposium on Radiation from Relativistic Electrons in Periodic Structures, 2007.
[9] T. Suwada, M. Satoh, K. Furukawa, T. Kamitani, T. Sugimura, K. Umemori, H. Okuno, Y. Endou, T. Haruna, R. Hamatsu, T. Sumiyoshi, K. Yoshida, A.P. Potylitsyn, I.S. Tropin, R. Chehab, First application of a tungstensingle-crystal positron source at the kek b factory, Phys. Rev. ST Accel. Beams 10 (7) (2007) 073501.
[10] X. Artru, R. Chehab, M. Chevallier, V. Strakhovenko, Advantages of axially aligned crystals used in positron production at future linear colliders, Phys. Rev. ST Accel. Beams 6 (9) (2003) 091003.
[11] W.P. GOU, G.X. PEI, Design of BEPCII positron source, Chin. Phys. C 26 (3) (2002) 279–285.
[12] A. Ushakov, G. Moortgat-Pick, S. Riemann, Undulator-based positron source at 250 GeV CM energy with different optical matching devices: Pulsed flux concentrator and quarter wave transformer, 2018.
[13] T. Kamitani, M. Akemoto, D.A. Arakawa, et al., SuperKEKB Positron source construction status, 2014.
[14] A. Thoma, K. Asmussen, R. Dux, et al., Plasma Phys. Control. Fusion 39 (1997) 1487;
A. Thoma, K. Asmussen, R. Dux, et al., Plasma Phys. Control. Fusion 39 (1997) 1487, Cracking.
[15] Y. Yuan, H. Greuner, K. Krieger, et al., Recrystallization and melting behavior of rolled tungsten under high heat flux loads, in: 2nd Sino–German Workshop on PWI in IPP, 2010;
N. Yoshida, H. Iwakiri, K. Tokunaga, et al., J. Nucl. Mater. 946 (2005) 337–339.
[16] G. Federici, Phys. Scr. (2006) T124;
B. Fu, W. Lai, Y. Yuan, et al., J. Nucl. Mater. 427 (2012) 268-273, [1] (1-3).
[17] K.D. Rasch, R.W. Siegel, H. Schultz, Phil. Mag. A 41 (1980) 91–117.
[18] R.D. Allen, L.F. Glasier, P.L. Jordan, J. Appl. Phys. 31 (1960) 1382;
D.K. Wagner, Phys. Rev. B 5 (1972) 336.
[19] P.K. Schelling, S.R. Phillpot, P. Keblinski, Phys. Rev. B 65 (2002) 144306.
[20] R.H. Xia, X.G. Tian, Y.P. Shen, Acta Mech. Sinaca 26 (2010) 599.
[21] A. Maiti, G.D. Mahan, S.T. Pantelides, Solid State Commun. 102 (1997) 517.
[22] P. Heino, E. Ristolainen, Microelectron. J. 34 (2003) 773.
[23] Z.H. Wang, Z.X. Li, Appl. Therm. Eng. 26 (2006) 2063.
[24] G.J. Wagner, R.E. Jones, J.A. Templeton, et al., Comput. Methods Appl. Mech. Engrg. 197 (2008) 3351.
[25] N. Mingo, L. Yang, D. Li, et al., Nano Lett. 3 (2003) 1713.
[26] Z.H. Wang, Z.X. Li, Appl. Therm. Eng. 26 (2006) 2063.
[27] A.R. Abramson, C.L. Tien, A. Majumdar, J. Heat Transfer 124 (2002) 963.
[28] S.G. Volz, G. Chen, Appl. Phys. Lett. 75 (1999) 2056.
[29] A.R. Abramson, C.L. Tien, A. Majumdar, J. Heat Transfer 124 (2002) 963.
[30] P.K. Schelling, S.R. Phillpot, P. Keblinski, Phys. Rev. B 65 (2002) 144306;
A. Maeda, Phys. Rev. E 52 (1995) 234.
[31] A. Maiti, G.D. Mahan, S.T. Pantelides, Solid State Commun. 102 (1997) 517.
[32] P. Heino, E. Ristolainen, Microelectron. J. 34 (2003) 773.
[33] M.W. Finnis, J.E. Sinclair, Phil. Mag. A 50 (1984) 45.
[34] M.W. Finnis, J.E. Sinclair, Phil. Mag. A 50 (1984) 45.
[35] F.C. Nix, D. MacNair, Phys. Rev. 61 (1942) 74.
[36] F.M. Plathe, J. Chem. Phys. 106 (1997) 6082.
[37] A. Maiti, G.D. Mahan, S.T. Pantelides, Solid State Commun. 102 (1997) 517.
[38] P.K. Schelling, S.R. Phillpot, P. Keblinski, Phys. Rev. B 65 (2002) 144306.
[39] Q. Xu, T. Yoshiie, H.C. Huang, Nucl. Instrum. Methods Phys. Res. Sect. B 206 (2003) 123–126.
[40] N.Y. Park, Y.C. Kim, H.K. Seok, S.H. Han, S. Cho, P.R. Cha, Nucl. Instrum. Methods Phys. Res. Sect. B 265 (2007) 547–552.
[41] J. Fikar, R. Schaeublin, Nucl. Instrum. Methods Phys. Res. Sect. B 255 (2007) 27–31.
[42] J. Fikar, R. Schaeublin, Nucl. Instrum. Methods Phys. Res. Sect. B 255 (2007) 27–31;
C. Bjorkas, K. Nordlund, Nucl. Instrum. Methods Phys. Res. Sect. B 259 (2007) 853–860.
[43] X.D. Dai, Y. Kong, J.H. Li, B.X. Liu, J. Phys.: Condens. Matter 18 (2006) 4527.
[44] B. Fu, B. Xu, W. Lai, et al., J. Nucl. Mater. 441 (1–3) (2013) 24–28.
[45] X.D. Dai, Y. Kong, J.H. Li, B.X. Liu, J. Phys.: Condens. Matter 18 (2006) 4527.
[46] B. Fu, B. Xu, W. Lai, et al., J. Nucl. Mater. 441 (1–3) (2013) 24–28.
[47] Y. Yuan, H. Greuner, B. B?Swirth, et al., Recrystallization and grain growth behavior of rolled tungsten under VDE-like short pulse high heat flux loads, J. Nucl. Mater. 433 (1–3) (2013) 523–530;
C.J.M. Denissen, et al., Int. J. Refract. Met. Hard Mater. 24 (2006) 321.
[48] G. Maddaluno, F. Pierdominici, M. Vittori, J. Nucl. Mater. 908 (1997).
[49] X. Liu, et al., J. Nucl. Mater. 687 (2004) 329–333.
[50] G. Pintsuk, I. Uytdenhouwen, Int. J. Refract. Met. Hard Mater. 28 (2010) 661.
[51] A. Zhitlukhin, et al., J. Nucl. Mater. 301 (2007) 363–365;
T. Tanabe, et al., Fusion Eng. Des. 275 (1998) 39–40, [7].
[52] S.E. Gustafsson, Transient plane source techniques for thermal conductivity and thermal diffusivity measurements of solid materials, Rev. Sci. Instrum. 62 (1991) 797–804.
[53] H. Zhang, Y.M. Li, W.Q. Tao, Theoretical accuracy of anisotropic thermal conductivity determined by transient plane source method, Int. J. Heat Mass Transfer 108 (part_PB) (2017) 1634–1644.
[54] S.E. Gustafsson, Transient plane source techniques for thermal conductivity and thermal diffusivity measurements of solid materials, Rev. Sci. Instrum. 62 (1991) 797–804.
[55] T. Log, S.E. Gustafsson, Transient plane source (TPS) technique for measuring thermal transport properties of building materials, Fire Mater. 19 (1995) 39–43.
[56] M. Gustavsson, E. Karawacki, S.E. Gustafsson, Thermal conductivity, thermal diffusivity and specific heat of thin samples from transient measurements with hot-disk sensors, Rev. Sci. Instrum. 65 (1994) 3856–3859.
[57] G. Maddaluno, F. Pierdominici, M. Vittori, J. Nucl. Mater. 908 (1997) 241–243;
X. Liu, et al., J. Nucl. Mater. 687 (2004) 329–333, [11].
[58] W.D. Klopp, W.R. Witzke, NASA Technical Note (TN D-3232), National Aeronautics and Space Administration, Washington, DC, USA, 1966.
[59] C.J.M. Denissen, et al., Int. J. Refract. Met. Hard Mater. 24 (2006) 321.
[60] L.M. Clareborough, M.E. Hargreaves, M.H. Loretto, Recovery and Recrystallization of Metals, Interscience, New York, 1963.
[61] A. Maiti, G.D. Mahan, S.T. Pantelides, Solid State Commun. 102 (1997) 517.
[62] Melt-layer ejection and material changes of three different tungsten materials under high heat-flux conditions in the tokamak edge plasma of TEXTOR, Nucl. Fusion 51 (11) (2011) 113020.

[63] S.X. Peng, A.L. Zhang, W.B. Wu, T.H. Ma, Y.X. Jiang, K. Li, H.T. Ren, T. Zhang, J.F. Zhang, Y. Xu, J.M. Wen, W.B. Wu, Z.Y. Guo, J.E. Chen, Plasma simulation and optimization for a miniaturized antenna ECR ion source, Nucl. Instrum. Methods Phys. Res. A (2021) 1011–165586.

[64] Y.C. Lin, D.X. Wen, M.S. Chen, et al., A novel unified dislocation density-based model for hot deformation behavior of a nickel-based superalloy under dynamic recrystallization conditions, Appl. Phys. A 122 (9) (2016) 805.

[65] A. Ayad, M. Ramoul, A. Rollett, et al., Quantifying primary recrystallization from EBSD maps of partially recrystallized states of an IF steel, Mater. Charact. (2020) 171.

[66] http://www.speciation.net/Database/Instruments/Oxford-Instruments/HKL-Channel-5-;i1153.

[67] W.B. Wu, A.L. Zhang, S.X. Peng, T.H. Ma, Y.X. Jiang, K. Li, H.T. Ren, T. Zhang, J.F. Zhang, Y. Xu, J.M. Wen, W.B. Wu, Z.Y. Guo, J.E. Chen. A. global model of, 2.45 GHZ ECR ion sources for high intensity H+, H2+ and H3+ beams, Vacuum (2020) 109744.

[68] A. Hn, B. Mk, A. Mk, et al., A design of an electron driven positron source for the internationallinear collider - ScienceDirect, Nucl. Instrum. Methods Phys. Res. A 953.

[69] V. BHARADWAJ, R. PITTHAN, J. SHEPPARED, et al., Design issues for ILC the positron source, in: C. HORAK (Ed.), Proceedings of the Particle Accelerator Conference, Institute of Electrical and Electronics Engineers, Inc, USA, 2005, pp. 3230–3232.